iScience

CellPress
OPEN ACCESS

Article

Nanophotonic color splitters for high-efficiency imaging

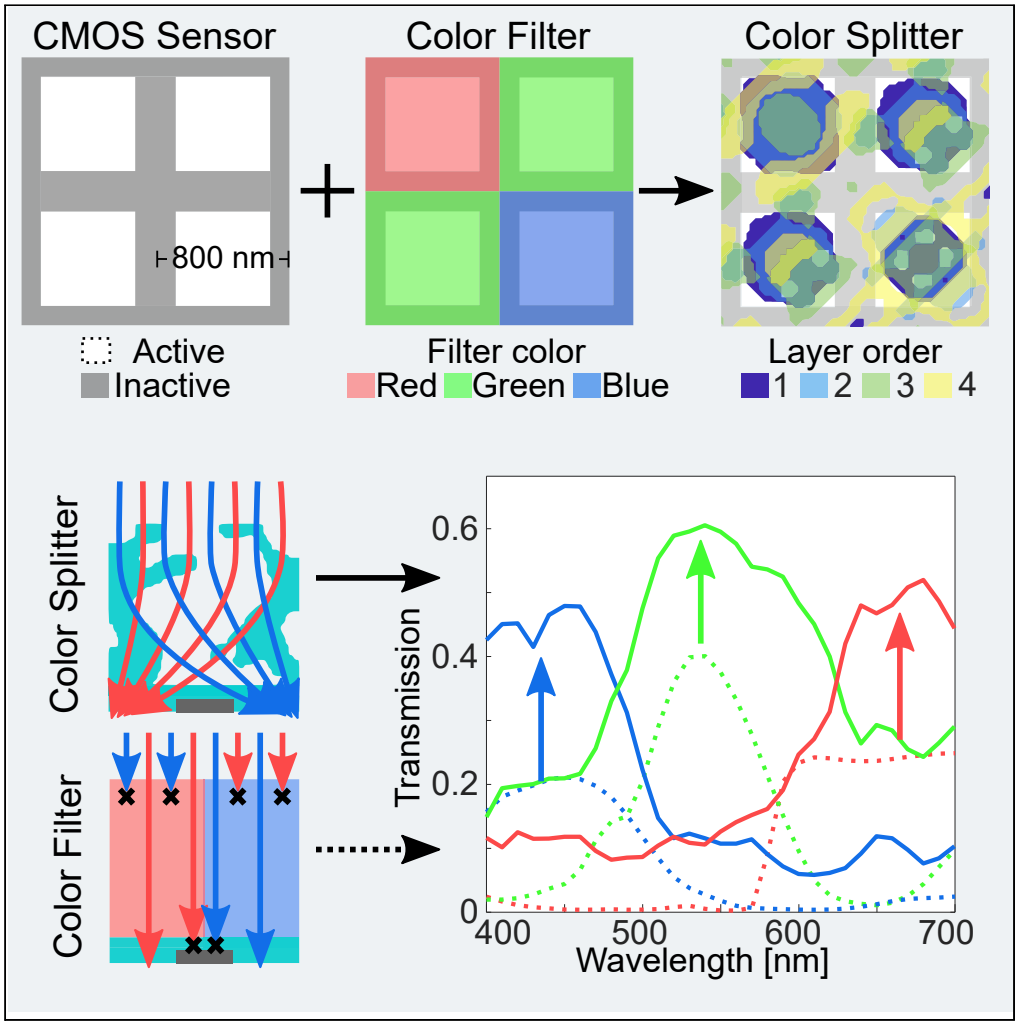

Eric Johlin

ejohlin@uwo.ca

Highlights

Color splitters focus and sort light into pixels without any absorptive losses

New single-material splitters are designed to sit directly on a CMOS sensor surface

Splitters with four or more layers show significant improvements over filters

Color-corrected and nearly lossless greyscale imaging can be done with one splitter

Johlin, iScience *24*, 102268
April 23, 2021
https://doi.org/10.1016/j.isci.2021.102268

iScience

CellPress
OPEN ACCESS

Article

Nanophotonic color splitters for high-efficiency imaging

Eric Johlin[1,2,*]

SUMMARY

Standard color imaging utilizes absorptive filter arrays to achieve spectral sensitivity. However, this leads to ~2/3 of incident light being lost to filter absorption. Instead, splitting and redirecting light into spatially separated pixels avoids these absorptive losses. Herein we investigate the inverse design and performance of a new type of splitter which can be printed from a single material directly on top of a sensor surface and are compatible with 800 nm sensor pixels, thereby providing drop-in replacements for color filters. Two-dimensional structures with as few as four layers significantly improve fully color-corrected imaging performance over standard filters, with lower complexity. Being fully dielectric, these splitters additionally allow color-correction to be foregone, increasing the photon transmission efficiency to over 80%, even for sensors with fill-factors of 0.5. Performance further increases with fully 3D structures, improving light sensitivity in color-corrected imaging by a factor of 4 when compared to filters alone.

INTRODUCTION

Color imaging is most commonly achieved through absorptive Bayer filter arrays (depicted in Figures 1A and 1C), with each of three color pixel filters allowing ~1/3 of the incident light to transmit to the active material below (Bayer, 1976). While this allows high selectivity of individual colors and thus simple image processing, the significant losses are becoming an increasing issue, particularly as the trend toward smaller, higher resolution sensors further reduces the incoming average photon count per pixel.

An alternative approach to filtering is splitting the incident light by color, redirecting the appropriate wavelength range to a corresponding pixel (Figure 1B). Theoretically, this can increase the photon collection on average by 3×, with additional improvements possible for front-illuminated CMOS configurations (where often only 50% of the illuminated surface is photoactive) (Zhang et al., 2010), due to built-in lensing/funneling (Sounas and Alu, 2016; Johlin et al., 2018). Color splitting for imaging applications has been investigated previously through fairly complex processes (Chen et al., 2016), often involving high-index material processing steps (Sounas and Alu, 2016; Miyata et al., 2019; Chen et al., 2017; Nishiwaki et al., 2013; Tamang et al., 2019; Zhao et al., 2020), new elements in the far-field of the sensor (Miyata et al., 2019; Chen et al., 2017; Nishiwaki et al., 2013; Xiao et al., 2016; Camayd-Muñoz et al., 2020), and computationally expensive image reconstructions (Wang and Menon, 2015; Sahoo et al., 2017). Many designs additionally only work with a specific polarization of light, limiting their efficiency for normal imaging applications (Xu et al., 2010; Nguyen-Huu et al., 2011; Kanamori et al., 2006). Furthermore, as sensors now regularly feature pixel sizes down to 800 nm in pitch (Sony Corporation, 2018), color splitters need to be capable of handling this high pixel density as well, which to our knowledge has not yet previously been achieved, with many existing designs being 10-100× larger (Davis et al., 2017; Wang and Menon, 2015; Chen et al., 2017).

In essence, there are three competing objectives for either color splitters or filters: selectivity, transmissivity, and simplicity. Filters excel at selectivity and simplicity, but with low transmissivity, while splitters usually sacrifice simplicity and selectivity for increased transmissivity. While selectivity can to some degree be compensated for via processing (Wang and Menon, 2015; Hauser et al., 2019), so far the need for multiple additional materials, as well as precisely aligned additional layers away from the sensor surface have precluded wide adoption of color splitters for compact sensing.

In this work, we computationally explore the design process and performance of fully dielectric, low-index nanophotonic color splitters for imaging applications, with the splitter element printed directly on the

[1]Western University, Mechanical and Materials Engineering, 1151 Richmond Street, London, N6A 3K7 ON, Canada

[2]Lead contact

*Correspondence: ejohlin@uwo.ca

https://doi.org/10.1016/j.isci.2021.102268

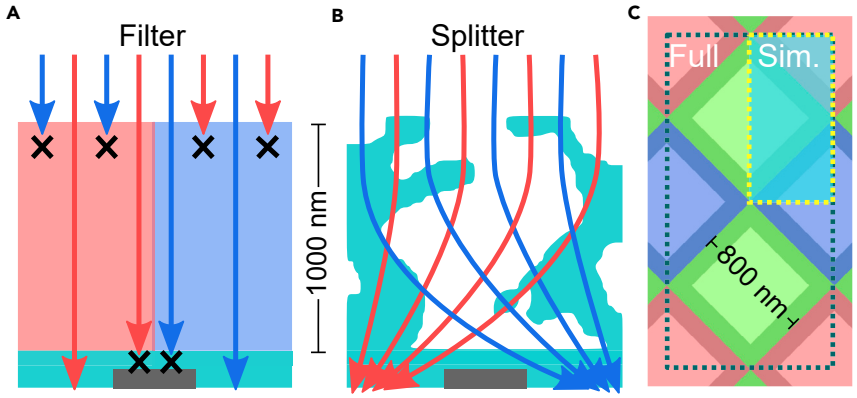

Figure 1. Schematic of working principle

(A) Cross-sectional diagram showing color filters (blue, red regions), which lose 50%–75% of incident light to the filter absorption, and can suffer additional losses due to inactive regions (gray bar) on the sensor front surface.

(B) Color splitters investigated here separate and focus light in the appropriate color pixel, obviating absorption loss, as well as the need for micro-lens arrays.

(C) Top view of a Bayer array, with colors corresponding to red, green, and blue color pixels, and the investigated splitter unit cell and actively simulated (through symmetry) regions outlined (dashed gray and yellow lines, respectively). The shaded regions represent the inactive sensor regions, with a 50% fill-factor.

surface (and thus in the near-field) of the active material layer. This would thereby allow these novel splitters to serve as simple drop-in replacements for the current absorptive filters, while significantly increasing the sensor transmissivity. Specifically, we investigate components containing a range of geometric complexity, from single-layer 2D patterns (producible through simple single-step photolithography) to fully 3D structures (fabricable through multi-photon lithography (Deubel et al., 2004), or holography (Yuan and Herman, 2016)). In all cases, we consider only a single low index ($n = 1.5$) dielectric material, printed directly on top of a complementary metal–oxide–semiconductor (CMOS) image sensor, which to our knowledge has not been investigated previously. We observe up to 2.0× improvements in photon collection efficiency even after rigorous (but computationally trivial) color correction, accompanied by the option to increase collection by 2.4× in grayscale imaging (e.g. for low-light imaging, night vision) on the same sensor.

RESULTS

Splitter design

The general philosophy of this work is to utilize adjoint-based inverse design to determine structures that succeed at splitting broadband, randomly polarized light into a pixel array, based on three distinct wavelength bands: 400-500 nm (blue), 500-600 nm (green), and 600-700 nm (red). We investigate structures of varying complexity, from single-layer (fully 2D; metasurface) coatings, to four-layer (4× 2D) coatings (Figures 2A and 2B), producible through one to four standard photolithography steps respectively, to fully 3D photonic-crystal-like structures (Figures 2C and 2D).

We utilize a two-step process for the overall design of the splitter geometry: First, topology optimization using a simple figure of merit is run for a range of initial conditions, returning a locally optimal structure for each provided starting point. This is followed by a more accurate analysis of the final designs, using a color-corrected efficiency metric to determine the single best structure those generated by the various initial conditions. The process for each of the steps follows, with additional details in the transparent methods.

Topology optimization

Adjoint-based inverse design is an efficient method for nanophotonic topology optimization (Rodriguez et al., 2018). This works by leveraging properly configured forward and reverse (adjoint) simulations to compute gradients of a figure of merit with respect to discrete changes in structural permittivity. By iterating this process, one can converge on a locally optimal solution to a figure of merit, given the initial conditions. This approach has been used widely in nanoscale optics to design components ranging from optical resonators (Lu et al., 2011), to integrated photonic circuits (Lalau-Keraly et al., 2013;

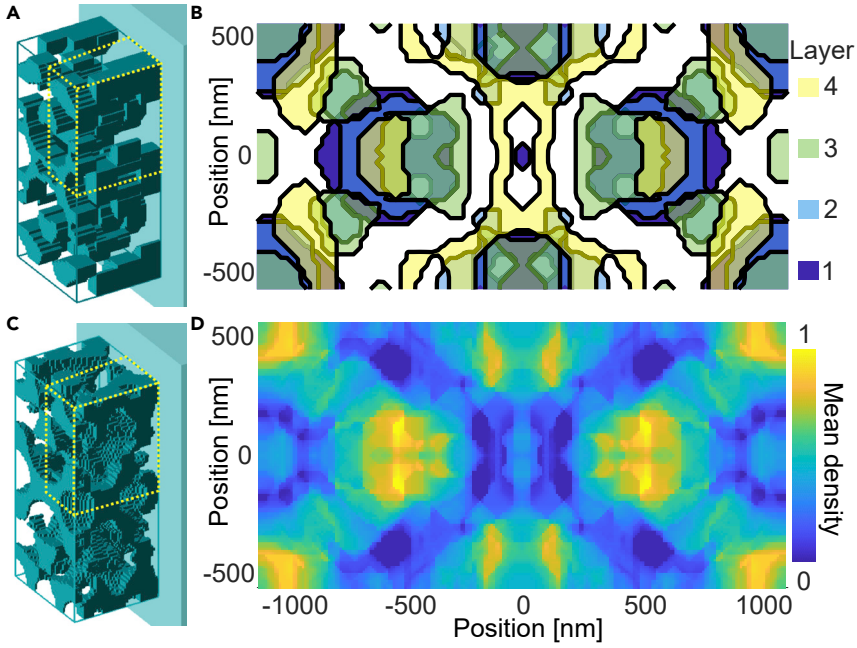

Figure 2. Color splitter designs

(A) Isometric-view rendering, and (B) top-view of color-coded layers for the four-layer topology-optimized splitter structure.

(C) Isometric view and (D) top-view average density projection of fully 3D splitter structure. Dashed yellow lines in A and C represent the actively simulated region.

Elesin et al., 2014; Piggott et al., 2015), to metasurfaces able to perform computational tasks (Estakhri et al., 2019; Liu et al., 2018).

Here, we utilize inverse design to maximize the concentration of on-band (correctly colored) light in the center of the corresponding pixel. Pixel sizes are fixed at 800 nm to correspond to the highest resolution CMOS detectors commonly available today (Sony Corporation, 2018), with an assumed active area fill-factor of 0.5, corresponding to 565 nm wide square active regions (Zhang et al., 2010). The optimization region total thicknesses was limited to 1000 nm, similar to the thickness of color filters (FUJIFILM Holdings, 2020). The material being structured is taken to be purely dielectric with a refractive index of $n = 1.5$ comparable to that of transparent photoresist, on a glass substrate of equivalent index, and with a background of air ($n = 1.0$) on the front surface and any material-absent areas of the structured region.

Each optimization iteration step consists of four broadband finite-difference time-domain simulations, corresponding to the two orthogonal light polarizations, each with one forward and one adjoint simulation. By orienting the simulation coordinate system diagonally with respect to the sensor layout, we can exploit the system symmetry, requiring only 1/4 of the splitter region to be actively simulated (dashed outlines in Figure 1C). For the 800 nm pixel size, the active simulation area thus has dimensions of 565 × 1130 nm.

The optimization figure of merit (FoM) is the function that the optimization takes gradients of to determine the evolution of the structure permittivity, and thus geometry. While ideally the final color-corrected response (discussed below) would be used for the optimization, such an equation is not differentiable making the computation of gradients impossible. To address this, we use a simplified FoM for the optimization, corresponding to the intensity of the electric field of on-band light ($|E|^2$) in the center of each color pixel immediately below the splitter surface, from broadband planewave illumination in the forward simulation. This corresponds to a simple adjoint simulation as well, corresponding to a single dipole emitter of the proper emission frequency again at the center of each pixel, scaled by the electric field from the forward simulation. This follows the general method of field localization optimization described in (Miller, 2012), and is coincidentally similar to method used by the concurrent work in (Camayd-Muñoz et al., 2020).

As adjoint-based topology optimizations are local optimization techniques, the choice of initial conditions have a significant impact on the resulting design and performance. For each layer complexity, a series of optimizations was run, ranging from fully filled to fully empty along with 9 equally spaced uniform index levels between as the starting point for the optimization. This allows us to utilize a full color-corrected efficiency calculation to compare the 11 resulting structures for each configuration and select those with the best overall performance. See the transparent methods supplemental document for additional details and Figure S1 for a flowchart of the optimization and simulation process.

Color-corrected efficiency

At the most basic level, a color splitter could be operated similar to a color filter, attenuating the incoming light to the point where the off-band color response (e.g. red light into the blue pixel region) is sufficiently low, and then determining the transmission efficiency of the on-band color response. However, since the signal from four single-color pixels are combined to create one RGB image pixel, one can use the correlations between the pixels to determine more accurately the colors in the image. This allows color selectivity to be improved, although still at a cost of some signal intenstiy. We here describe a general method for evaluating the overall color imaging efficiency using a simple matrix inversion process, applicable to any color isolating component (splitter or filter).

We begin by creating a 3 × 3 matrix, $\mathbf{R}$ of the color response, with rows corresponding to the red, green, and blue pixels, and columns being the average red, green, and blue color transmission into the respective pixel. In a theoretically perfect splitter, $\mathbf{R}$ would be the identity matrix, but in any real design there will be some degree of off-color transmission represented by non-zero off-diagonal elements. The inverse of the response matrix represents the linear combination of the pixel responses that would recover the identity matrix ($\mathbf{I}$) and thus the ideal response, by using combinations of the color pixels to effectively cancel out the off-band responses. However, in order to avoid amplification of noise, the value of any element in the inverse matrix must be limited to 1 (*i.e.* we allow signal attenuation but not gain). Furthermore, the total performance of the system will be ultimately limited by the response of the worst-performing color-corrected element, and so the color responses must be uniformly scaled. We thus normalize the inverse matrix by the largest element in said matrix, thereby providing the gain-free color-correction matrix, $\mathbf{Q}$, as

$$\mathbf{Q} = \frac{\left(\mathbf{R}^{-1}\right)}{\max\left[\left|\mathbf{R}^{-1}\right|\right]}. \qquad \text{(Equation 1)}$$

The color-corrected response to a uniform input is thus $\mathbf{RQ}$, and is equal to $\eta\mathbf{I}$, where η is the overall color-corrected efficiency.

It should be noted that while matrix inversion is often a computationally expensive process, the small 3 × 3 size of these response matrices, and the need for this to be performed only once during the splitter design phase makes the color correction process computationally trivial – during actual imaging, the correction is simply a uniform linear combination of the sensor's red, green, and blue signals.

Performance of splitters

The highest splitter performance was achieved by the fully 3D structures. The structure is portrayed in Figures 2C and 2D, and the color response is shown in Figure 3, with the Poynting vector components normal to the substrate at surface (representing the flux of energy) depicted in Figure 3B. It can be seen that all three colors are not only spatially isolated, but well focused into the center of the active region of the corresponding pixel, even without micro-lens arrays. The four-layer structure (shown in Figures 2A and 2B) appears similar in spatial power transmission (Figure 3A), still showing strong spectrally selective focusing of light onto the sensor surface. The selectivity, however, is slightly lower, particularly for the green pixel, as seen in Figure 3C.

The simulated transmission spectrum is shown in Figure 3C and D for four-layer and 3D splitters, respectively, and is compared to that of a representative commercial Bayer filter absorptive layers (FUJIFILM Holdings, 2020). It is observed that each color component of collection efficiency is higher than that of absorptive filters, indicating that light is successfully rerouted into the correct filter region. This is likely occurring through a combination of refractive and interference effects, allowing efficient broadband responses to be created in the near-field of the sensor (Johlin et al., 2018). It also can be noted that while the collection efficiency is much higher, the selectivity is lower. However, as discussed above, this can be compensated for using linear combinations of the color pixel readings via Equation 1 to produce the

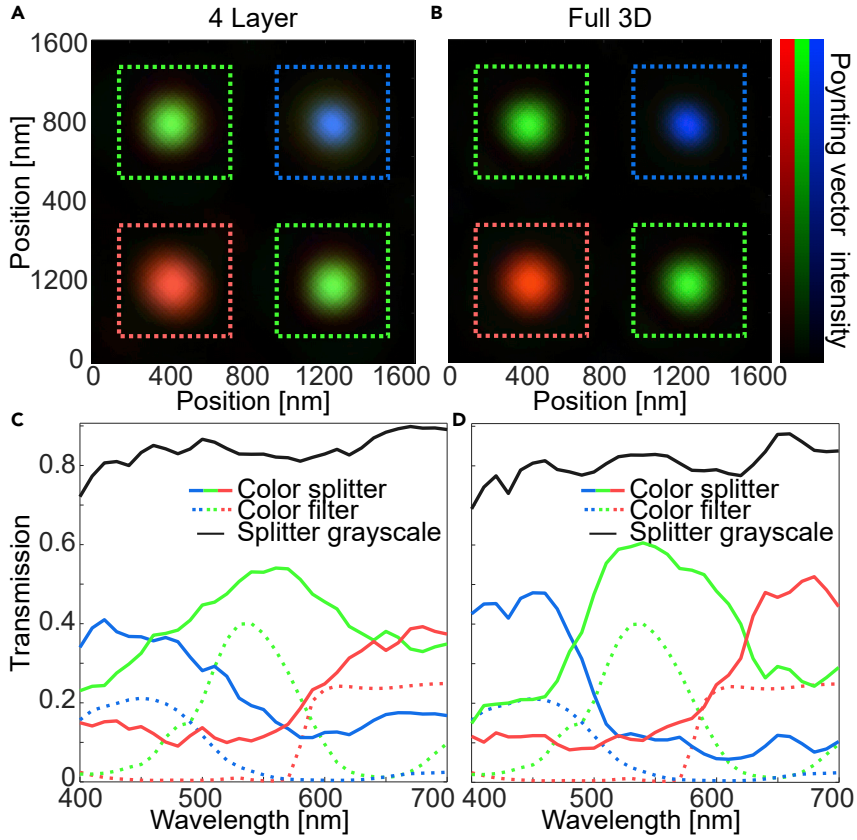

Figure 3. Splitter operation

(A) Poynting vector $\hat{z}$-component (toward the sensor) within the three color bands (red, green, blue), visualized at the sensor surface. Pixel active regions are shown as dashed lines.

(B) Transmission of light from the full 2 × 2 pixel region into the sensor active region for the three different pixel colors. The 3D splitter (solid lines) shows lower selectivity than the Bayer filter (dashed lines), but the much higher transmissivity still leads to twice the color-corrected efficiency (34% *vs.* 17%, respectively).

final fully color-corrected image, at a cost of some sensitivity. Our estimated efficiency of the 3D color splitter is 34% for fully color-corrected imaging, and 81% for grayscale imaging. This is compared to the Bayer filter, with color-corrected estimated efficiency of 17%, and grayscale efficiency of 33%.

Interestingly, the color separation mechanism of the splitters investigated herein appears to be distinct from those largely studied previously; the proximity of the color splitting structure prevents the use of angular redistribution to spectrally separate the light (Nishiwaki et al., 2013), relying instead on full spatial separation at the base of the splitter, with little redistribution in angular-space of the transmitted light. This provides additional benefits as well, in that the splitters designed here appear to perform better at off-angle illumination than previous designs that rely more on scattering or diffraction to reconfigure the angular distribution from the splitter (Camayd-Muñoz et al., 2020). For full characterization of these effects, see Figure S4.

Simulated full-color imaging

In order to validate the accuracy of the color correction, as well as visualize the increased sensitivity, it is instructive to directly compare the performance of the two sensor designs (Bayer filter *vs.* splitter) on realistic images. To do this, we use freely available 2000 × 2000 pixel hyperspectral images (Brainard, 2004) to simulate the operation of both the 3D color splitter, as well as the Bayer array for comparison. Through convolution of the per-pixel spectrum, first with a light source spectrum (the AM 1.5 sunlight spectrum is used here), followed by our color responses, and finally applying the linear color correction operation from Equation 1, we obtain the expected full-color image response for each design. A reference image

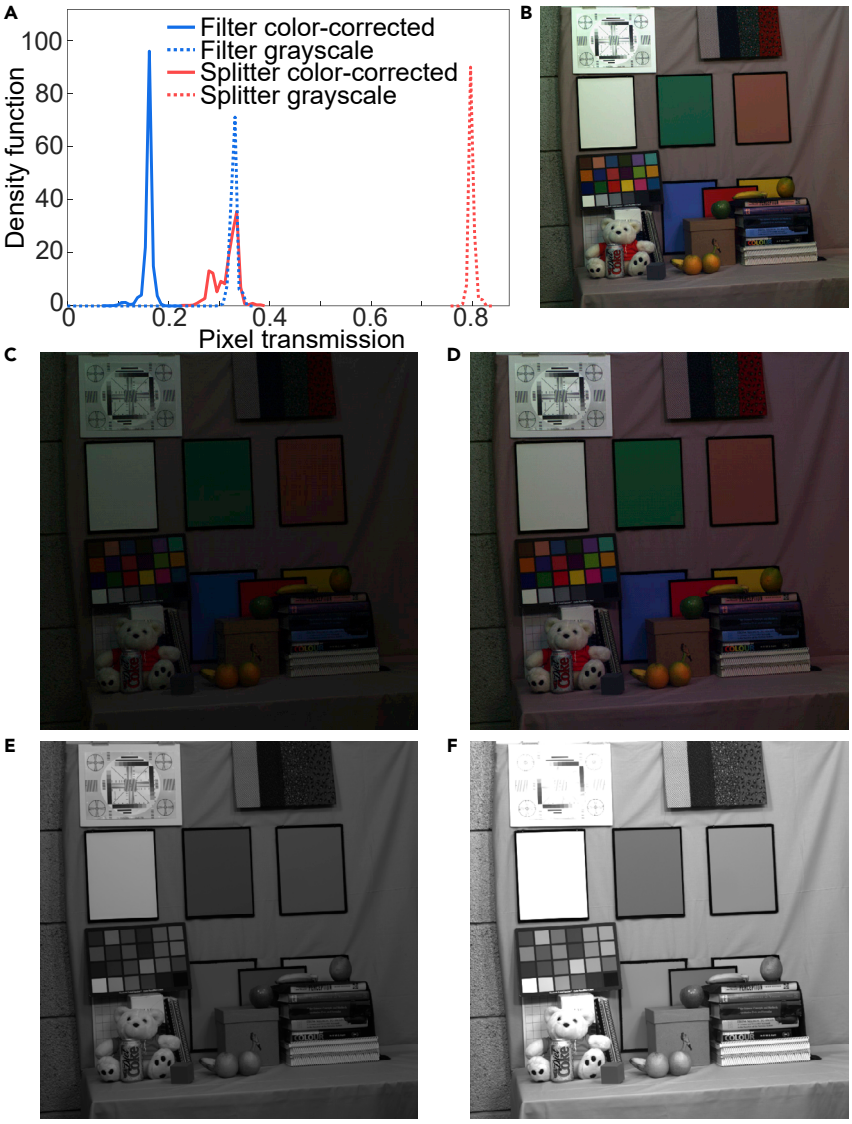

Figure 4. Simulated imaging response

(A) Pixel transmission density functions for color splitters (red) and Bayer filters (blue), in color-corrected (solid) and grayscale (dashed) imaging, for the given test image.

(B) Reference image assuming perfect splitting at 50% efficiency.

(C and D) Color-corrected simulated images for comparing filter and splitter performance, respectively.

(E and F) Grayscale simulated images for filter and splitter, respectively.

with 50% efficiency and perfect color separation is shown in Figure 4B, along with the responses of filters and splitters after color correction, as well as in grayscale imaging.

By comparing the color-corrected response of the filter (Figure 4C) and splitter (Figure 4D) to the reference image, the splitters accurately reproduce the true colors, and with higher brightness than the standard Bayer filter. This is increasingly visible in the grayscale images (Figures 4E and 4F), where the splitter even surpasses the brightness of the 50% efficiency reference image. From the imaging efficiency distributions in Figure 4A, we can see that indeed in color imaging the collection efficiency is increased by a factor of 2.0, from 15.9% for the Bayer filter to 31.3% for the color splitter, and with the grayscale efficiency increasing by a factor of 2.4, from 33.6% to 80.2%. The difference in performance from the estimated efficiency arises the non-uniform color distribution of the reference image, responsible for the extended distribution in the splitter transmission density function as well.

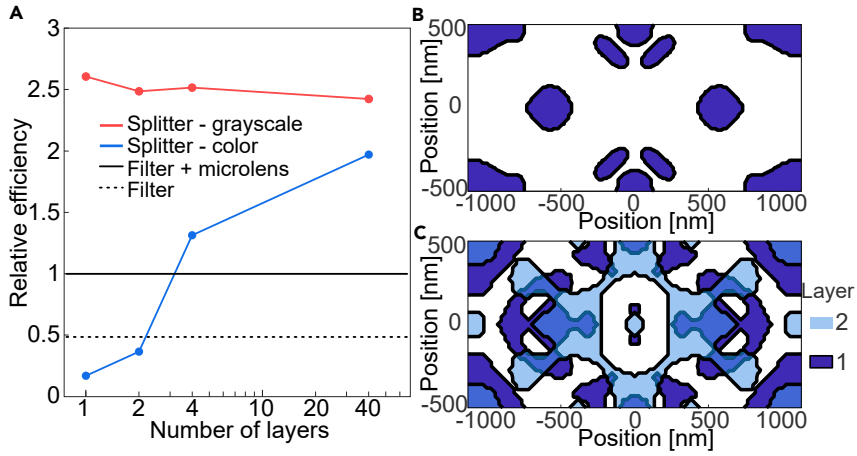

Figure 5. Performance vs. complexity trade-off

(A) Splitter performance, in terms of relative color-corrected imaging efficiency, shown for both in color (blue) and grayscale (red) imaging. Performance is normalized to Bayer filters with assumed perfect micro-lens structures (black solid), with the performance without such lenses shown as well (black dashed).

(B and C) Single- and two-layer structure geometries are shown in B and C, respectively.

Furthermore, the above comparisons all conservatively assume perfect micro-lens structures above the Bayer filter array, being both lossless and focusing all transmitted light into the active region. Without micro-lens arrays, the Bayer filter efficiency would be reduced by an additional factor of 2, with imperfect lenses somewhere in between. The splitters require no such micro-lens arrays, as they inherently focus the light into the active regions already.

It should be noted that the color correction used here is strict, in that all cross-color response must be eliminated. This is why even the Bayer filters, which have some color contamination, particularly in the green pixel response, show reduced efficiency when corrected as well. By limiting the strictness of this correction, any position on the trade-off continuum from no color correction to full color correction can be selected, and so for lower color contrast, increasing efficiencies can be realized.

Complexity and robustness

Reducing the layer complexity by an order of magnitude to just four discrete layers (structure shown in Figures 2A and 2B), still maintains much of the performance of the color splitters. In fully color-corrected imaging, an efficiency of 21% is obtained, still notably higher than filters, especially when compared to filters without micro-lens arrays. In grayscale imaging, performance is even slightly higher than full 3D splitters, at 83%. With two layers (Figure 5C), or even just a single-layer (Figure 5B), splitters are still able to produce full-color images, although at a fairly low efficiency. As expected, they maintain high grayscale performance, still without the need for any micro-lens array.

This trend in performance *vs.* complexity is further clarified in Figure 5A, showing the simulated color-corrected imaging efficiency with respect to the number of splitter layers. It should be noted that fully 3D structures here are equivalent to 40-layer structures due to the finite optimization voxel size. In particular the large gain in performance between two- and four-layer configurations is clearly visible, with the imaging efficiency moving from substantially below the filter performance, to substantially above. This leap in performance indicates that the distinct layers spectrally separate light as it moves through the splitter, and demonstrating that the changes in structure topology (as splitter thickness is constant) progressively separates and focuses the three color bands. Further characterization of one- and two-layer splitter structures is shown in Figure S2.

Finally, in order for such color splitters to be usable in real devices, robustness against both defects and non-ideal operating conditions should be ensured. Due to the broadband response of the splitters, performance should be generally invariant to minor (uniform) expansion or contraction of the structure. Furthermore, the strong focusing within the active regions of the pixels allows some built-in robustness to misalignment, as shown in Figures 3A and 3B, and quantified in Figure S3. While all analysis here assumes randomly polarized light, we

additionally ensure that such splitters perform well in arbitrary linear polarizations, as well as for non-normal incident light, as is common in normal imaging systems (see Figures S4–S6).

DISCUSSION

Herein we have shown that efficient color splitters can be designed using low-index dielectric layered 2D or fully 3D structures directly on the surface of CMOS sensors. Performance significantly surpasses that of traditional filter arrays for splitter designs even with as few as four layers, with efficiency enhancements as high as 4 times over CMOS sensors without micro-lens arrays. Splitter structures show added functionality in the ability to choose any point in the color accuracy *vs.* sensitivity trade-off, permitting accurate color imaging, nearly lossless grayscale imaging, and anything in between, all on the same sensor. This could offer particular advantages in color biological imaging, where high efficiency, small pixel sizes, and color sensitivity are all desired (Wu et al., 2008; Farsiu et al., 2004). Furthermore, these splitter structures do not require any focusing micro-lens arrays, even when used with 800 nm pixel CMOS sensor configurations with active area fractions of 50%, further simplifying the use of such components.

The placement of the splitter in the near-field of the sensor surface offers unique benefits over previous color splitter configurations as well, both in design and performance. Removing the need for precise yet thick separation layers can simplify fabrication, and operating without angular redistribution of light transmitted to the sensor surface appears to provide increased invariance to off-normal illumination conditions, and may also reduce losses and cross talk in sensor as well (Zhang et al., 2010).

Finally, the color-corrected efficiency metric developed for the splitter design process here is general, and should be useful in comparing the performance of new splitter or filter structures as well. A similar design and analysis approach could additionally be utilized for other applications, such as infrared imaging or multi-junction photovoltaics, especially where splitting and focusing are both advantageous (Xiao et al., 2016).

Limitations of the study

All work presented here is computational, and so limitations and adjustments to designs may be necessary when experimentally fabricating such splitters. The structures discussed here are intended to be fabricable through either sequential photolithography (for layered structures), or printed directly with multi-photon lithography (Deubel et al., 2004). While feature sizes were specifically limited to allow reasonable (with the smallest features having 90 nm widths), the same process with either more or less restrictive limitations on sizes, numbers of layers, or a different refractive index material could be implemented as needed. The built-in robustness against expansion/contraction of the structures, as well as slight misalignments should ease fabrication requirements; however misalignment between layers of 2D structures could also hinder performance. Concurrent work by others has demonstrated the operation of 3D dielectric splitters (although with larger overall sizes, and positioned far above a sensor surface) in the microwave regime (Camayd-Muñoz et al., 2020), providing evidence that structured splitter devices should be readily achievable in the near future.

Resource availability

Lead contact

Further information and requests should be directed to the Lead Contact, Dr. Eric Johlin (ejohlin@uwo.ca).

Materials availability

This study did not use or generate any physical materials.

Data and code availability

The data that support the findings of this study are available from the corresponding author upon reasonable request.

METHODS

All methods can be found in the accompanying transparent methods supplemental file.

SUPPLEMENTAL INFORMATION

Supplemental information can be found online at https://doi.org/10.1016/j.isci.2021.102268.

ACKNOWLEDGMENTS

The author thanks Dr. Olga Trichtchenko (Western University, Canada) for helpful discussions. This work was partly supported by the Natural Sciences and Engineering Research Council of Canada (NSERC).

DECLARATION OF INTERESTS

The authors declare no competing interests.

Received: December 11, 2020
Revised: January 8, 2021
Accepted: February 28, 2021
Published: April 23, 2021

REFERENCES

Bayer, B.E. (1976). Color Imaging Array (US Patent), p. US3971065A.

Brainard, D.H. (2004). Hyperspectral image data. http://color.psych.upenn.edu/hyperspectral/.

Camayd-Muñoz, P., Ballew, C., Roberts, G., and Faraon, A. (2020). Multifunctional volumetric meta-optics for color and polarization image sensors. Optica *7*, 280–283.

Chen, B.H., Wu, P.C., Su, V.C., Lai, Y.C., Chu, C.H., Lee, I.C., Chen, J.W., Chen, Y.H., Lan, Y.C., Kuan, C.H., et al. (2017). Gan metalens for pixel-level full-color routing at visible light. Nano Lett. *17*, 6345–6352.

Chen, Q., Hu, X., Wen, L., Yu, Y., and Cumming, D.R. (2016). Nanophotonic image sensors. Small *12*, 4922–4935.

Davis, M.S., Zhu, W., Xu, T., Lee, J.K., Lezec, H.J., and Agrawal, A. (2017). Aperiodic nanoplasmonic devices for directional colour filtering and sensing. Nat. Commun. *8*, 1347.

Deubel, M., Von Freymann, G., Wegener, M., Pereira, S., Busch, K., and Soukoulis, C.M. (2004). Direct laser writing of three-dimensional photonic-crystal templates for telecommunications. Nat. Mater. *3*, 444–447.

Elesin, Y., Lazarov, B.S., Jensen, J.S., and Sigmund, O. (2014). Time domain topology optimization of 3D nanophotonic devices. Photon. Nanostructures *12*, 23–33, https://doi.org/10.1016/j.photonics.2013.07.008.

Estakhri, N.M., Edwards, B., and Engheta, N. (2019). Inverse-designed metastructures that solve equations. Science *363*, 1333–1338, https://doi.org/10.1126/science.aaw2498.

Farsiu, S., Robinson, D., Elad, M., and Milanfar, P. (2004). Advances and challenges in super-resolution. Int. J. Imaging Syst. Technology *14*, 47–57.

FUJIFILM Holdings (2020). RGB primary color filters for image sensor applications: 5th generation color mosaic. https://www.fujifilm.com/us/en/business/semiconductor-materials/image-sensor-color-mosaic/rgb/applications.

Hauser, J., Golub, M.A., Averbuch, A., Nathan, M., Zheludev, V.A., Inbar, O., and Gurevitch, S. (2019). High-photon-throughput snapshot colour imaging using a monochromatic digital camera and a pupil-domain diffuser. J. Mod. Opt. *66*, 710–725.

Johlin, E., Mann, S.A., Kasture, S., Koenderink, A.F., and Garnett, E.C. (2018). Broadband highly directive 3d nanophotonic lenses. Nat. Commun. *9*, 1–8.

Kanamori, Y., Shimono, M., and Hane, K. (2006). Fabrication of transmission color filters using silicon subwavelength gratings on quartz substrates. IEEE Photon. Technology Lett. *18*, 2126–2128.

Lalau-Keraly, C.M., Bhargava, S., Miller, O.D., and Yablonovitch, E. (2013). Adjoint shape optimization applied to electromagnetic design. Opt. Express *21*, 21693, https://doi.org/10.1364/oe.21.021693.

Liu, D., Tan, Y., Khoram, E., and Yu, Z. (2018). Training deep neural networks for the inverse design of nanophotonic structures. ACS Photon. *5*, 1365–1369, https://doi.org/10.1021/acsphotonics.7b01377.

Lu, J., Boyd, S., and Vučković, J. (2011). Inverse design of a three-dimensional nanophotonic resonator. Opt. Express *19*, 10563, https://doi.org/10.1364/OE.19.010563.

Miller, O.D. (2012). Photonic Design: From Fundamental Solar Cell Physics to Computational Inverse Design (Ph.D. thesis.).

Miyata, M., Nakajima, M., and Hashimoto, T. (2019). High-sensitivity color imaging using pixel-scale color splitters based on dielectric metasurfaces. ACS Photon. *6*, 1442–1450.

Nguyen-Huu, N., Lo, Y.L., and Chen, Y.B. (2011). Color filters featuring high transmission efficiency and broad bandwidth based on resonant waveguide-metallic grating. Opt. Commun. *284*, 2473–2479.

Nishiwaki, S., Nakamura, T., Hiramoto, M., Fujii, T., and Suzuki, M. (2013). Efficient colour splitters for high-pixel-density image sensors. Nat. Photon. *7*, 240.

Piggott, A.Y., Lu, J., Lagoudakis, K.G., Petykiewicz, J., Babinec, T.M., and Vučković, J. (2015). Inverse design and demonstration of a compact and broadband on-chip wavelength demultiplexer. Nat. Photon. *9*, 374–377, https://doi.org/10.1038/nphoton.2015.69.

Rodriguez, A.W., Lin, Z., Vučković, J., Jin, W., Molesky, S., and Piggott, A.Y. (2018). Inverse design in nanophotonics. Nat. Photon. *12*, 659–670, https://doi.org/10.1038/s41566-018-0246-9.

Sahoo, S.K., Tang, D., and Dang, C. (2017). Single-shot multispectral imaging with a monochromatic camera. Optica *4*, 1209–1213.

Sony Corporation (2018). Sony releases stacked CMOS image sensor for smartphones with industry's highest 48 effective megapixels. https://www.sony.net/SonyInfo/News/Press/201807/18-060E/.

Sounas, D.L., and Alu, A. (2016). Color separation through spectrally-selective optical funneling. ACS Photon. *3*, 620–626.

Tamang, A., Parsons, R., Palanchoke, U., Stiebig, H., Wagner, V., Salleo, A., and Knipp, D. (2019). Color sensing by optical antennas: approaching the quantum efficiency limit. ACS Photon. *6*, 2041–2048.

Wang, P., and Menon, R. (2015). Ultra-high-sensitivity color imaging via a transparent diffractive-filter array and computational optics. Optica *2*, 933–939.

Wu, C., Bull, B., Szymanski, C., Christensen, K., and McNeill, J. (2008). Multicolor conjugated polymer dots for biological fluorescence imaging. ACS Nano *2*, 2415–2423.

Xiao, T.P., Cifci, O.S., Bhargava, S., Chen, H., Gissibl, T., Zhou, W., Giessen, H., Toussaint, K.C., Yablonovitch, E., and Braun, P.V. (2016). Diffractive spectral-splitting optical element designed by adjoint-based electromagnetic

optimization and fabricated by femtosecond 3D direct laser writing. ACS Photon. *3*, 886–894, https://doi.org/10.1021/acsphotonics.6b00066.

Xu, T., Wu, Y.K., Luo, X., and Guo, L.J. (2010). Plasmonic nanoresonators for high-resolution colour filtering and spectral imaging. Nat. Commun. *1*, 59.

Yuan, L.L., and Herman, P.R. (2016). Laser scanning holographic lithography for flexible 3d fabrication of multi-scale integrated nano-structures and optical biosensors. Scientific Rep. *6*, 22294.

Zhang, F., Zhang, J., Yang, C., and Zhang, X. (2010). Performance simulation and architecture optimization for cmos image sensor pixels scaling down to 1.0 μm. IEEE Trans. Electron Devices *57*, 788–794.

Zhao, N., Catrysse, P.B., and Fan, S. (2020). Perfect rgb-ir color routers for sub-wavelength size cmos image sensor pixels. Adv. Photon. Res. *2*, 2000048, https://doi.org/10.1002/adpr.202000048.

iScience, Volume *24*

Supplemental information

Nanophotonic color splitters for high-efficiency imaging

Eric Johlin

Transparent Methods

Inverse Design

Inverse design is performed through topology optimization using a modified version of the Lumopt package (Lalau-Keraly et al., 2013). Broadband (400–700 nm wavelength) simulations are utilized to exploit the efficiency of FDTD techniques with large spectral ranges, and to preclude the need for an additional simulation for each wavelength range. Ideally, under broadband, planewave illumination, all light of each wavelength range would be perfectly focused onto the center of the corresponding pixel, with no spectral overlap between pixels. This is represented in the optimization by the forward (400-700 nm planewave illumination) and adjoint (3× dipoles, each with a 80 nm wavelength range centered in the 100 nm color band to reduce spectral overlap, located at the pixel center) simulations.

Full 3D optimizations allow each volume element of the predefined structure region to be independently modified. For 2D and layered structures, the spatial gradients are averaged in the direction orthogonal to the 2D design plane, allowing the mean performance in the optimization region to determine the direction of the optimization. Optimization are performed using a limited-memory Broyden–Fletcher–Goldfarb–Shanno algorithm with bound constraints (L-BFGS-B), as implemented in Scipy (Van Der Walt et al., 2011). The software utilizes built-in hyperparameters to converge both the binarization of the permittivity (begins with continuous values of permittivity, and moves to either material present or absent) as well as maximum radius of curvature of the structures (set to 100 nm to be compatible with 3D nano-lithography) (Johlin et al., 2018; Deubel et al., 2004). The optimization finishes with a binarization threshold of 99%, and gradients at a relative magnitude of 10^{-4}.

Each color pixel provides it's own value of the figure of merit (FoM), with the total simply corresponding to the sum of the three color components. The minimum is not used as again, the FoM operation must be differentiable for the optimization to correctly compute gradients. However, it is still important to bias the optimization toward improving the worst-performing color pixel. To do so, between line-search steps in the optimization (at the same time that penalty functions for discreetness and curvature are implemented) a uniform linear weighting, equal to the reciprocal of the individual color performances from the previous optimization round, is applied to each of the three color components. This allows the increased weighting of the lower

performing color components without introducing errors in the gradient computations.

Layer complexities of one-, two-, and four-layer structures, and fully 3D structures (equivalent to 40 layers due to the 25 nm pixel size) were individually optimized. Layered structures do not enforce minimum feature size limitations between layers.

Simulations

Simulations are performed using FDTD Solutions (Lumerical Inc.) Optimization is done using a mesh size of 25 nm in all directions in the optimization region, and 31 equally-spaced wavelength points. The optimization region sits immediately on top of a glass substrate, with the figure of merit measured at one grid point below the surface.

The forward simulation uses the magnitude of the electric field at the center of the pixel as the figure of merit. After optimization, final structures are simulated at a higher resolution grid of 10 nm, and fully binarized to ensure no gradient index material remains from the optimization.

Design Process Flowchart

A flowchart of the full inverse design process is shown in Fig. S1.

Lower-Complexity Structures

The structure of the lower-complexity one- and two-layer configurations are shown in Fig. 5 **b** and **c** of the main text. The full thickness of all splitter configurations is fixed at 1000 nm, with the layers equally spaced within this domain. Here we further characterize these lower complexity structures.

The optical responses of the lowest complexity single- and two-layer structures are displayed in Fig. S2. The Poynting vector images in Fig. S2 **a, b** show the enhanced color separation as layer complexity increases, visible through the increasingly pure color focus spot at the center of the pixel active regions. The transmission responses in Fig. S2 **c, d** similarly show improved color isolation with increasing number of layers, especially when moving to the four-layer design (Fig. 3**a** of the main text).

While single-layer structures provide very limited selectivity and contrast, the response of the different color pixels is still distinct enough to allow the color correction method to be employed, allowing color imaging (although at low sensitivity) with even these exceedingly simple structures. Moving to two layers improves this performance significantly, with trends in imaging performance shown in Fig. 5**a** of the main text.

Design Robustness

The broadband response of the structures designed here inherently provides some robustness to fabrication defects. Because of the scale invariance of Maxwell's equations, an overall dilation or contraction of the structures should result in simply a proportional shift in the color response. The broad responses, spanning 100 nm wavelength per color-band, suggest that such issues would be minimal.

Furthermore, the design is fairly robust against alignment issues as well; the plots of Poynting vector magnitude (the integral of which provides the power transmission; Fig. S2, and Fig. 3 of the main text) demonstrate that slight misalignment of the array would still lead to the vast majority of power being centered in the corresponding pixel. This power concentration is further clarified in Fig. S3, where we observe that the transmission in each pixel is highly confined to the central region, with full-widths at half-max between 200 nm and 250 nm for the transmissions using the 3D structure.

In terms of sensitivity to misalignment, for the four-layer splitter for example, the red pixel (with the widest distribution of the three colors) still contains 97% of the collected light in a 400 nm diameter central region of the pixel, and 90% in the central 275 nm diameter. This suggests that even with a misalignment of 145 nm, collection efficiency should fall by less than 10%. If the fill-factor of the CMOS detector is greater than 0.5, this sensitivity is even more robust, allowing larger misalignment while maintaining high efficiency.

Angular Response

As light incident on a photodetector in any real imaging system is not perfectly columnated, the response of the system to non-normal incoming light is important to consider. Here we compute the expected angular response for incoming light with off-normal angles ranging from 0 to 20 degrees.

For specific angular responses, the metric of color imaging efficiency is not particularly meaningful; any real image pixel will receive a distribution of angles, and so the need to image entirely with a single angular response is unfeasible. This would thus produce a meaningless color-correction inversion matrix and imaging efficiency. Instead, we here calculate the sorting efficiency, defined as the fraction of on-band incoming light entering the correct active region. This allows the relative performance under increasingly non-normal incident light to be compared, as well as comparisons to be made to

previous works employing a similar metric (although without a limited active sensor region)(Camayd-Muñoz et al., 2020).

From Fig. S4 we can see the performance of the three color band responses (corresponding to the red, blue, and two green pixels), relative to their normal response. From Fig. S4**a**, it can be seen that performance will likely be limited by the red pixel response (for angles $< 12°$), but with a relative sorting efficiency still greater than 0.5. This compares positively to relative angular sorting efficiencies of previous color splitters which have utilized significant gaps between the splitter and sensor surface.(Camayd-Muñoz et al., 2020) This is likely indeed due to the increased proximity of the splitter to the sensor limits the displacement of the focal spot, and thereby reduces the harmful impact of non-normal incident light on the splitter performance.

Interestingly, the four-layer splitter structure in Fig. S4**b** shows even better relative angular performance, not falling below a 0.5 relative sorting efficiency, even for incoming light angles as high as 20°. This indicates that in real imaging applications, the decreased performance between the fully 3D and layered 2D structures is reduced.

This is further elucidated in Fig. S4**c**, showing the absolute sorting efficiency of the two configurations. The limiting color response (red or blue, depending on angle and configuration) is still above even the normal-incidence limiting response of the perfectly focused color Bayer filter (sorting efficiency of 0.18 for blue pixels, from Fig. 3**c,d** of the main text), shown as the gray solid line for reference. Note that in reality, the assumption of perfectly ideal microlens arrays for the color filters will be further overly optimistic, meaning this response will in reality be significantly lower (and thus the splitters perform better by even a larger margin). Furthermore, particularly for the red and blue pixels, the active regions represent only 12.5% of the sensor surface, and so even at significant angles of incoming light, the emission is still being substantially focused into the correct region – the defocused limit (assuming all non-reflected light is spread evenly on the sensor) is shown as the dashed gray line.

The transmission into the active regions for three off-normal angles are shown in Fig. S5, for both 3D (**a-c**) and four-layer 2D structures (**d-f**). It can be seen that while selectivity decreases as the angle of incoming light increases, even at 16° incidence there is still some selectivity present. The total capture of light (grayscale transmission) is interestingly superior in the four-layer structure for high angle of incidence light, indicating that while spectral selectivity is decreased, the light focusing by the structures still is

maintained. Even at an incoming angle of 16°, over 75% of light is transmitted into the 0.5 fill-factor sensor regions. The ability of all structures to maintain high overall transmittance, even for significant angles of incoming light is likely due to the spatial separation of light at the base of these structures, in contrast to the angular separation (and reliance on multi-micrometer gaps) of those studied previously.

Polarization Response

While all responses shown in the main text assume randomly polarized incoming light (*i.e.* a uniform distribution of polarization angles), in some cases there may be a significant degree of linear polarization of the incoming light, and then the polarization response of the splitter becomes important. In Fig. S6 investigate the specific response of the two main splitter designs to two separate orthogonal linear polarizations of incoming light.

From Fig. S6 **a** and **b**, it can be seen that green response is slightly higher in **a**, red and blue are slightly higher in **b**, but the overall efficiency and contrast are largely similar between the two orthogonal conditions for the 3D splitter design. Specifically, the average sorting efficiency for polarization **a** is 44%, and for polarization **b** is 48%. Similarly in Fig. S6**c** and **d**, there is a slight difference in efficiency of red and blue response, but again overall efficiency and contrast are similar, with average sorting efficiencies of 41% and 37% for polarizations **a** and **b**, respectively. This indicates that even ,in situations where imaging is performed with linearly polarized incoming light (even with arbitrary unknown polarization angle), efficient color imaging can be performed using the splitter structures.

Direction of Energy Transmission

The color splitters explored here are designed to be printed directly on a sensor surface (and thus in the near-field of the sensor), but there is potential for the transmitted energy to have significant off-normal angular components, particularly as light is collected from a large region and transmitted into a small focal area. While we only consider the contribution of Poynting vector components in the surface normal direction when analyzing the transmission of the color splitters, significant components in other directions could contribute to energy loss, and thereby decreased efficiency of the systems.

In Fig. S7 we quantify these off-normal components, showing the energy probability density of the three light color bands for two splitter structures with respect to their angle from the surface normal. Each line indicates the

probability density for different Poynting vector angles of the energy within the correct color band and pixel active area at the sensor surface. A delta function at zero would thus correspond to all energy propagating perfectly normal to the surface (equivalent to the planewave input), while the more extended the distribution, the higher prevalence of off-angle contributions to the energy at the surface of the sensor. In both Fig. S7 **a** and **b** (3D and four-layer splitters, respectively) it can be seen that for all three colors have extremely narrow distributions, with over 90% of energy contained at angles of less than 0.5°. This fits well with the high performance observed in transmission of the splitter structures, as higher angle contributions would be seen as losses in our calculations. This also suggests that possibly including two red pixels (as opposed to two green pixels) would be more efficient for these designs, due to the increased difficulty in focusing and maintaining narrow angular transmission distributions of longer wavelength light.

The narrow angular distribution of these devices is also in direct contrast to the performance of previous splitter structures, which largely rely on diffractive(Nishiwaki et al., 2013) or scattering(Camayd-Muñoz et al., 2020) to intentionally redistribute different spectral bands of light into different angles to facilitate splitting. This indicates that the design of splitters directly the sensor surface does not only modify the configuration, but also preferences the design toward a different mechanism of operation as well.

Figure S1. Flowchart depicting inverse design process, Related to Supplemental Methods.

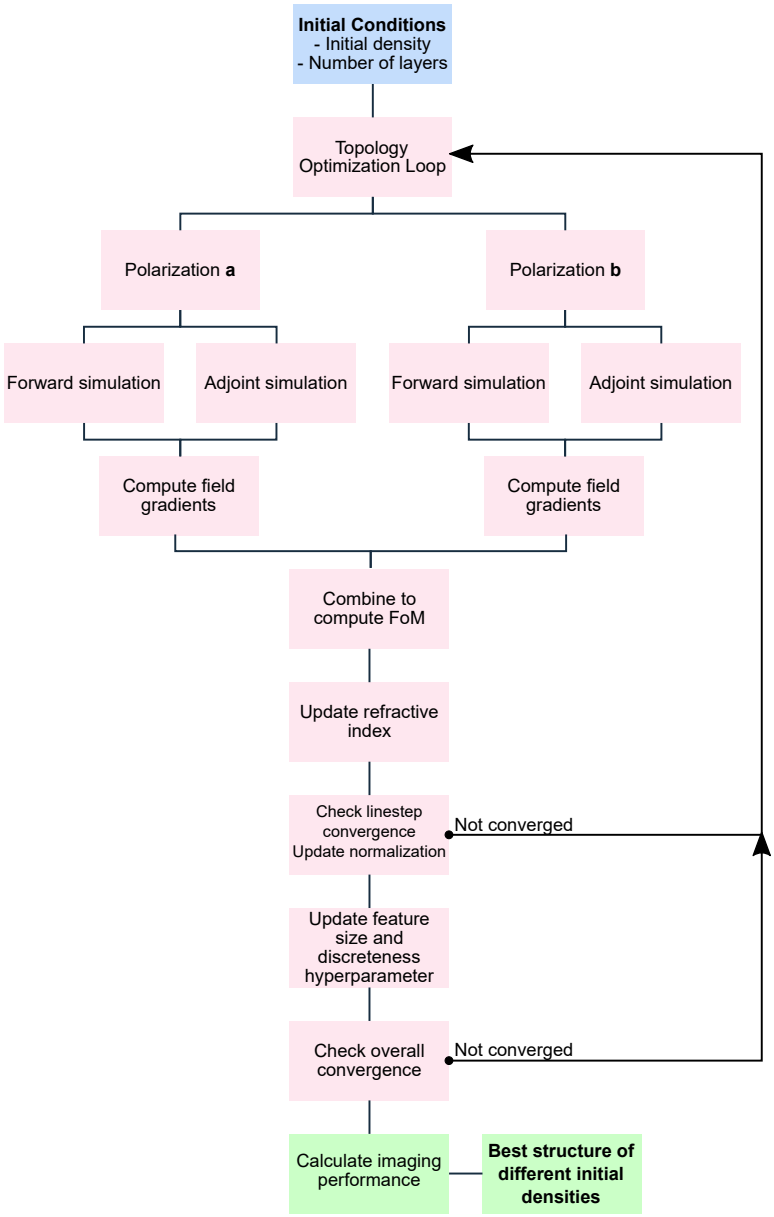

Figure S1: Initial conditions (e.g. layered vs. fully 3D structure, initial relative starting density from 0 to 1) are chosen (blue), and the topology of the given structure is optimized (red). This is then compared to the full performance of other structures with different starting conditions to find the globally best performing structure (although not necessarily the global optimum; green).

Figure S2. Color splitter performance, Related to Figure 3, Figure 5, Supplemental Methods.

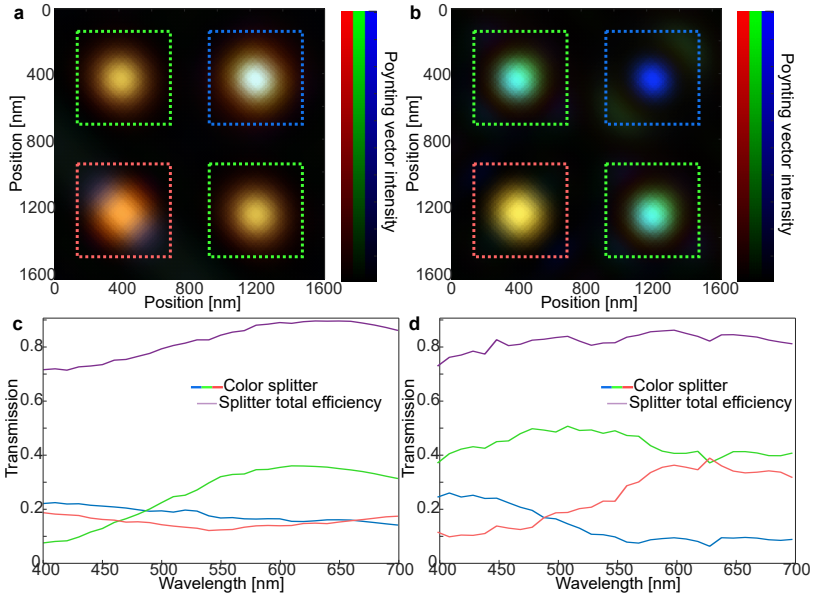

Figure S2: Poynting vector intensity into the sensor surface, integrated over the three 100 nm color bands (blue – 400-500 nm, green – 500-600 nm, red – 600-700 nm), for one- and two–layered structures (**a, b**, respectively). Integrated transmission into the corresponding color pixel active region, for one- and two-layered structures (**c, d**, respectively).

Figure S3. Spatial distribution of power transmission, Related to Figure 3, Figure 5, Supplemental Methods.

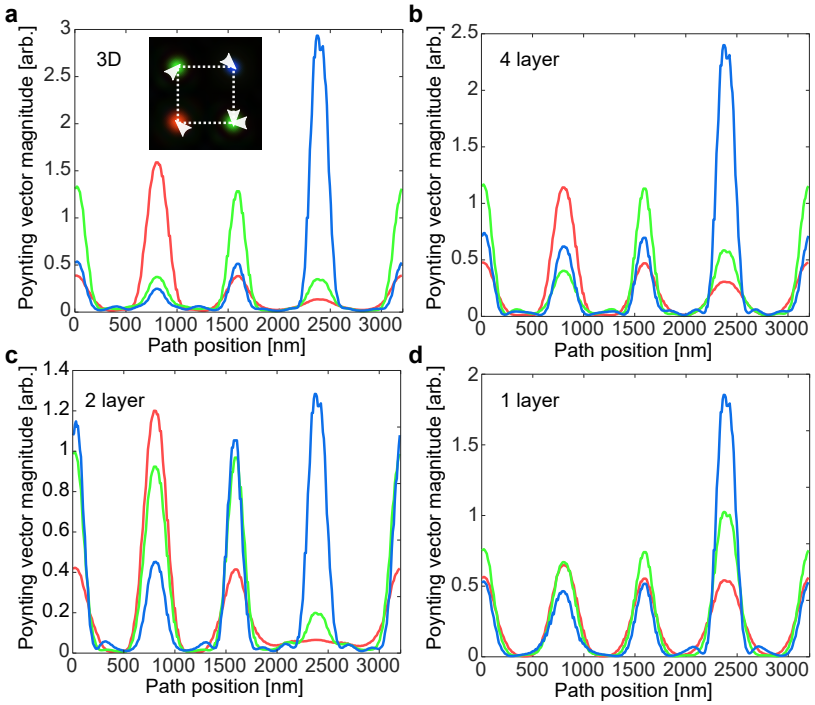

Figure S3: Path slices of the three color bands (blue, green and red lines) shown for one-, two-, and four-layer structures, as well as fully 3D structures, in **a, b, c,** and **d**, respectively. The path taken by the line traces is shown inset in **a**.

Figure S4. Angular response of splitter structures, Related to Figure 3, Supplemental Methods.

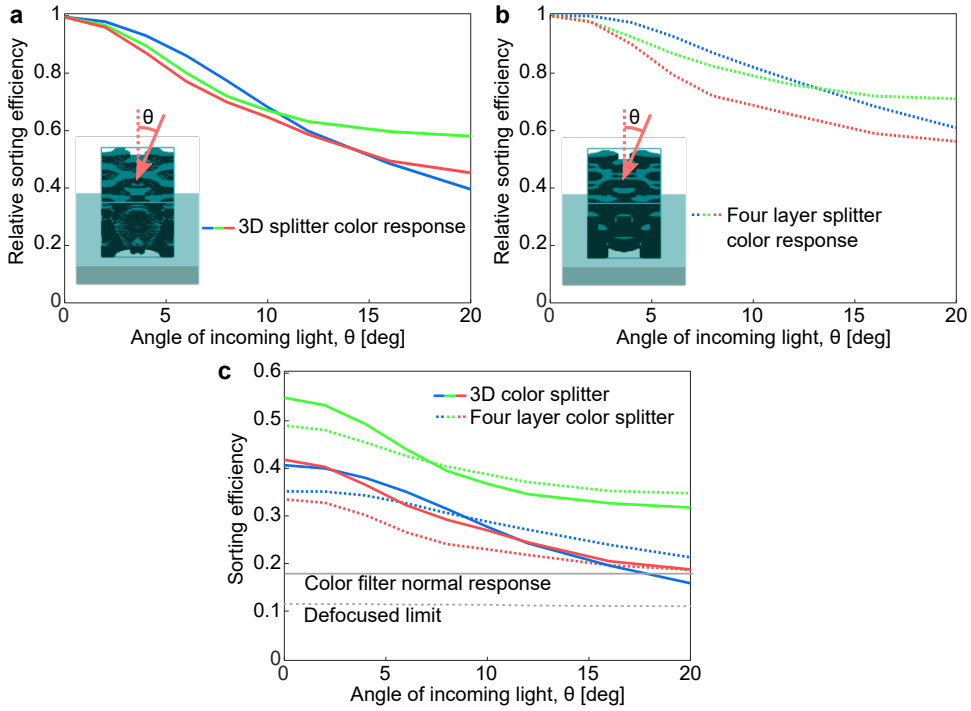

Figure S4: The relative sorting efficiencies for fully 3D as well as four-layer 2D structures with respect to the angle of incoming light, θ (depicted in the inset diagram) are shown in **a** and **b**, respectively. Absolute sorting efficiencies are shown in **c**, along with the corresponding limits for no focusing of light, as well as the limiting performance of color Bayer filters as the horizontal gray dashed and solid lines, respectively. The line colors (red, green, blue) correspond to the respective color pixels.

Figure S5. Color transmission for off-normal incidence light, Related to Figure 3, Supplemental Methods.

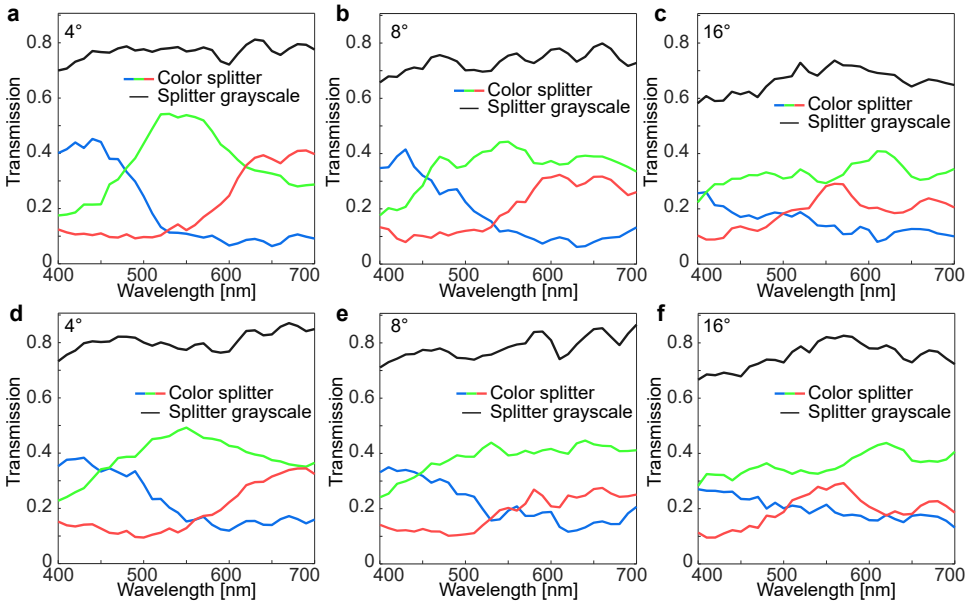

Figure S5: Transmission spectra into the three pixel color active regions, for fully 3D splitters are shown in **a-c**, and for four-layer 2D structures in **d-f**, for angles of 4°, 8°, and 16°, corresponding to the angle θ as depicted inset in Fig. S4. Line colors (red, green, blue) correspond to the respective color pixels, and black lines represent overall grayscale efficiency (the sum of the three color components).

Figure S6. Polarized response, Related to Figure 3, Supplemental Methods.

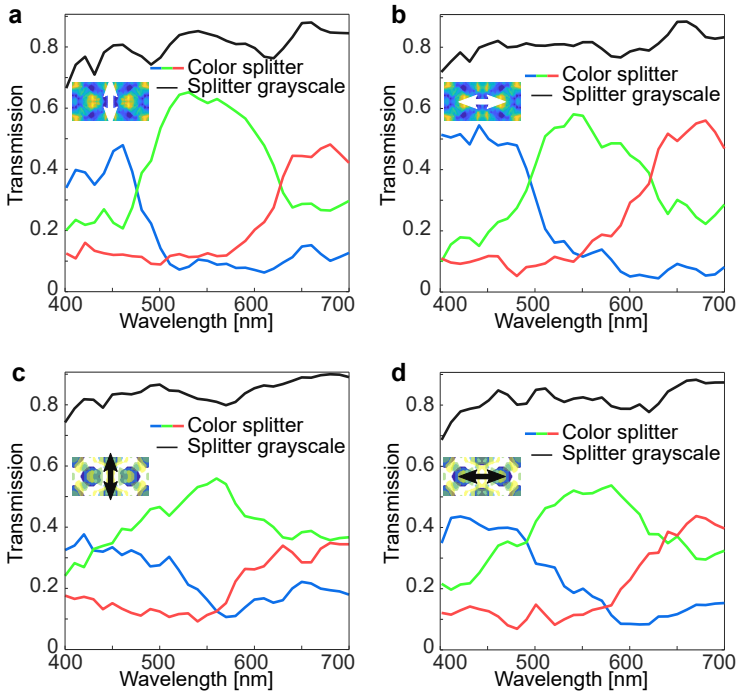

Figure S6: Specific transmission for two orthogonal linearly polarizations of light are shown in **a** and **b** for fully 3D splitters, and **c** and **d** for four-layer 2D splitter structures. Line colors (red, green, blue) correspond to the respective color pixels, and black lines represent overall grayscale efficiency (the sum of the three color components). Electric field polarization relative to the splitter structure is shown inset in each plot.

Figure S7. Angular transmission, Related to Figure 3, Supplemental Methods.

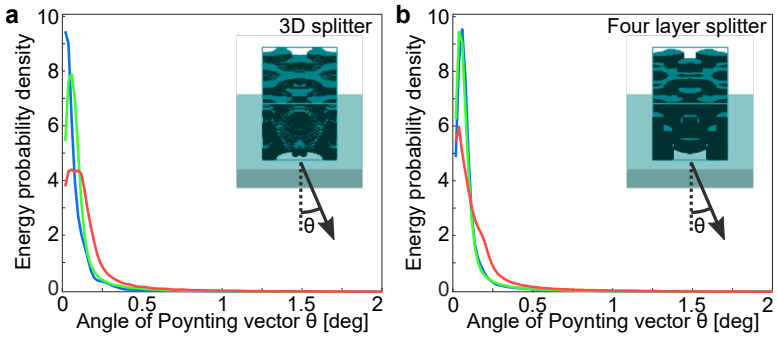

Figure S7: Energy probability density functions of Poynting vector angles (θ) with respect to the sensor surface normal. Fully 3D splitter response is shown in **a**, while four-layer 2D structure response is shown in **b**. Probability densities are normalized so that they integrate to one. Line colors (red, green, blue) correspond to the respective color pixels region and color band included in the calculation.

Supplemental References

Camayd-Muñoz, P., Ballew, C., Roberts, G., Faraon, A., 2020. Multifunctional volumetric meta-optics for color and polarization image sensors. Optica 7, 280–283.

Deubel, M., Von Freymann, G., Wegener, M., Pereira, S., Busch, K., Soukoulis, C.M., 2004. Direct laser writing of three-dimensional photonic-crystal templates for telecommunications. Nature Materials 3, 444–447.

Johlin, E., Mann, S.A., Kasture, S., Koenderink, A.F., Garnett, E.C., 2018. Broadband highly directive 3d nanophotonic lenses. Nature Communications 9, 1–8.

Lalau-Keraly, C.M., Bhargava, S., Miller, O.D., Yablonovitch, E., 2013. Adjoint shape optimization applied to electromagnetic design. Optics Express 21, 21693. doi:10.1364/oe.21.021693.

Nishiwaki, S., Nakamura, T., Hiramoto, M., Fujii, T., Suzuki, M., 2013. Efficient colour splitters for high-pixel-density image sensors. Nature Photonics 7, 240.

Van Der Walt, S., Colbert, S.C., Varoquaux, G., 2011. The numpy array: a structure for efficient numerical computation. Computing in Science & Engineering 13, 22.